HHS Public Access

Author manuscript

Cell Rep. Author manuscript; available in PMC 2024 February 16.

Published in final edited form as:

Cell Rep. 2023 November 28; 42(11): 113384. doi:10.1016/j.celrep.2023.113384.

Pathway-specific alterations in striatal excitability and cholinergic modulation in a SAPAP3 mouse model of compulsive motor behavior

Jeffrey M. Malgady[1,2], **Alexander Baez**[1,3], **Zachary B. Hobel**[1,2], **Kimberly Jimenez**[1], **Jack Goldfried**[1], **Eric M. Prager**[1], **Jennifer A. Wilking**[1], **Qiangge Zhang**[5], **Guoping Feng**[5,6], **Joshua L. Plotkin**[1,4,7,*]

[1]Department of Neurobiology & Behavior, Stony Brook University Renaissance School of Medicine, Stony Brook, NY 11794, USA

[2]Graduate Program in Neuroscience, College of Arts & Sciences, Stony Brook University, Stony Brook, NY 11794, USA

[3]Medical Scientist Training Program, Renaissance School of Medicine, Stony Brook University, Stony Brook, NY 11794, USA

[4]Center for Nervous System Disorders, Stony Brook University, Stony Brook, NY 11794, USA

[5]Yang Tan Collective and McGovern Institute for Brain Research, Department of Brain and Cognitive Sciences, Massachusetts Institute of Technology, Cambridge, MA 02139, USA

[6]Stanley Center for Psychiatric Research, Broad Institute of MIT and Harvard, Cambridge, MA 02142, USA

[7]Lead contact

SUMMARY

Deletion of the obsessive-compulsive disorder (OCD)-associated gene SAP90/PSD-95-associated protein 3 (*Sapap3*), which encodes a postsynaptic anchoring protein at corticostriatal synapses, causes OCD-like motor behaviors in mice. While corticostriatal synaptic dysfunction is central to this phenotype, the striatum efficiently adapts to pathological changes, often in ways that expand upon the original circuit impairment. Here, we show that SAPAP3 deletion causes non-synaptic and pathway-specific alterations in dorsolateral striatum circuit function. While somatic excitability was elevated in striatal projection neurons (SPNs), dendritic excitability was exclusively enhanced in direct pathway SPNs. Layered on top of this, cholinergic modulation was altered in opposing ways: striatal cholinergic interneuron density and evoked acetylcholine release

*Correspondence: joshua.plotkin@stonybrook.edu.

AUTHOR CONTRIBUTIONS

Conceptualization, J.M.M. and J.L.P.; investigation and analysis, J.M.M., A.B., Z.B.H., K.J., J.G., J.A.W., and E.M.P.; supervision and generation of SAPAP3 $cKT^{-/-}$ mice, Q.Z. and G.F.; writing, J.M.M. and J.L.P.; supervision and analysis, J.L.P.

DECLARATION OF INTERESTS

The authors declare no competing interests.

SUPPLEMENTAL INFORMATION

Supplemental information can be found online at https://doi.org/10.1016/j.celrep.2023.113384.

were elevated, while basal muscarinic modulation of SPNs was reduced. These data describe how SAPAP3 deletion alters the striatal landscape upon which impaired corticostriatal inputs will act, offering a basis for how pathological synaptic integration and unbalanced striatal output underlying OCD-like behaviors may be shaped.

Graphical Abstract

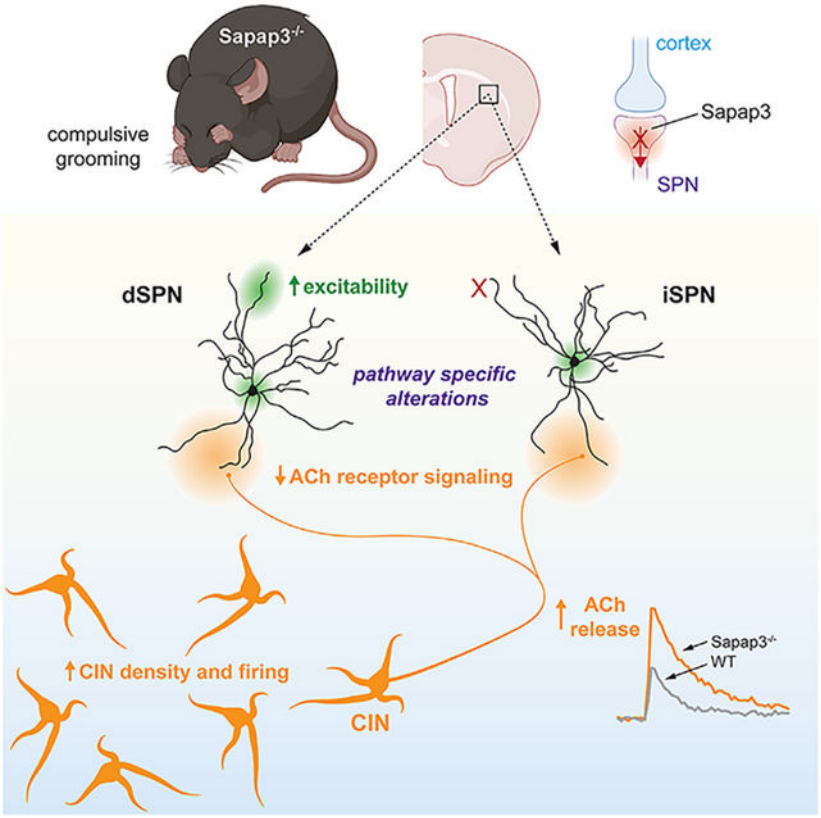

In brief

Malgady et al. show that deleting the OCD-associated gene *Sapap3* in mice leads to both elevated acetylcholine release and cell-specific attenuation of cholinergic signaling in output neurons of the dorsolateral striatum. This occurs alongside pathway-specific alterations in dendritic excitability that are expected to promote action initiation.

INTRODUCTION

The compulsive motor symptoms of obsessive-compulsive disorder (OCD) have been attributed to abnormal activity of the cortex-basal ganglia-thalamus-cortex loop.[1–5] The striatum, the main input nucleus of the basal ganglia, is considered to play an especially central role given that (1) it receives inputs from multiple cortical regions implicated in OCD,[1] (2) it is overactive in patients,[6,7] and (3) its normal function involves selecting and setting the urgency of competing motor commands,[8–10] processes that are impaired in OCD. The striatum is composed of two types of striatal projection neurons (SPNs), which provide

the structure's sole output to other nuclei of the basal ganglia: direct pathway SPNs (dSPNs) and indirect pathway SPNs (iSPNs).[8,9] While action selection involves coordinated activity of both pathways, engagement of dSPNs is associated with action initiation and engagement of iSPNs with action suppression.[11,12] Accordingly, circuit models of OCD posit that information flow through the basal ganglia is biased toward the direct pathway.[6,7,13]

Mounting evidence suggests that glutamatergic signaling is impaired in OCD.[7,14–16] In fact, numerous genes associated with OCD encode proteins that shape postsynaptic glutamate responses, and deletion of these genes in mice induces robust OCD-like motor behaviors such as excessive grooming.[17–20] Among these OCD-associated genes is SAP90/PSD-95-associated protein 3 (SAPAP3), which encodes a postsynaptic scaffolding protein enriched at corticostriatal synapses.[4,21–24] SAPAP3 knockout (KO) mice display impaired corticostriatal synaptic function, including reduced AMPA-receptor-mediated postsynaptic responses and elevated surface expression of and signaling through metabotropic glutamate receptor 5 (mGluR5) in SPNs.[20,25,26] While there is ample evidence for input specificity of corticostriatal synaptic alterations,[27–30] evidence for pathway (dSPN vs. iSPN) specificity of synaptic impairments is scant.[29] This is especially surprising considering that cortically driven striatal activity is pathologically biased toward the direct pathway in SAPAP3 KOs,[31] and pathway-specific optogenetic or chemogenetic manipulation of SPN activity can rescue compulsive grooming behavior in mice lacking either SAPAP3 or its postsynaptic binding partner Shank3.[32,33]

Given the extensive overlap of cortical inputs to dSPNs and iSPNs, it is unclear how deletion of SAPAP3 leads to relative changes in striatal output pathway activity. One clue comes from the finding that blocking mGluR5 signaling can "re-balance" the relative cortically evoked engagement of dSPNs vs. iSPNs in SAPAP3 KOs.[31] Though the mechanism underlying this pathway re-balancing is unclear, given that pathological mGluR5 signaling is observed in both dSPNs and iSPNs,[25,26] it raises the possibility that abnormal glutamatergic signaling induces additional local circuit alterations.[31] Here, we show that constitutive deletion of SAPAP3 leads to intrinsic alterations in SPN excitability and neuromodulation. While the somatic excitability of both dSPNs and iSPNs increased in the dorsolateral striatum of symptomatic mice, dendritic excitability was exclusively enhanced in dSPNs, shifting the normal balance away from the indirect pathway and toward the direct pathway. In addition to changes in intrinsic SPN excitability, we found that SAPAP3 deletion induces a hypercholinergic state in the dorsal striatum, as measured by increases in striatal cholinergic interneuron (CIN) density, basal CIN firing rate, and evoked acetylcholine (ACh) release. The elevation in cholinergic tone was paralleled by decreased responsivity of SPNs to ACh, in pathway-specific ways, as well as augmented muscarinic modulation of presynaptic glutamate release. Together, these data suggest that deletion of SAPAP3 induces intrinsic alterations in striatal circuitry that will shape how it responds to impaired cortical input.

RESULTS

Constitutive deletion of SAPAP3 leads to pathway-specific changes in striatal SPN intrinsic excitability

To determine whether deletion of SAPAP3 leads to non-synaptic pathway-specific alterations in SPNs, we generated a conditional variant of the SAPAP3 KO mouse (referred to here as SAPAP3 conditional knockin [*cKI*]$^{-/-}$) that constitutively lacks SAPAP3 expression and displays robust compulsive grooming behaviors beginning at ~3 months of age (Figure S1). Consistent with the previously reported SAPAP3 KO mouse model,[20] these mice also display elevated anxiety-like behavior (Figures S1G–S1I). We focused our study on striatal output neurons residing in the dorsolateral striatum, the region of the striatum most closely associated with habit learning and habitual behaviors in mice[34–38] and known to contain corticostriatal synaptic deficits in SAPAP3 KO mice.[20,26,30] To identify dSPNs and iSPNs, we crossed SAPAP3 *cKI*$^{-/-}$ mice with either drd1-tdTomato or drd2-EGFP mice[39,40] to label dSPNs and iSPNs, respectively. Unlike the central "associative" striatum, where deletion of SAPAP3 has no effect on SPN somatic excitability,[28] deletion of SAPAP3 significantly enhanced SPN excitability in the dorsolateral striatum (Figure 1). Both dSPNs and iSPNs displayed increased intrinsic somatic excitability, as measured by steeper current-voltage (IV) relationships (Figures 1A and 1B; two-way repeated measures ANOVA; *dSPN* $p < 0.0001$, $F(32,320) = 6.715$, wild type [WT] n = 18, SAPAP3 *cKI*$^{-/-}$ n = 16; *iSPN* $p < 0.0001$, $F(32,320) = 6.677$, WT n = 15, SAPAP3 *cKI*$^{-/-}$ n = 19); increased firing frequencies in response to depolarizing current injections (Figure 1C; two-way repeated measures ANOVA; *dSPN* $p < 0.0001$, $F(28,280) = 14.20$, WT n = 19, SAPAP3 *cKI*$^{-/-}$ n = 12; *iSPN* $p < 0.0001$, $F(39,390) = 11.37$, WT n = 22, SAPAP3 *cKI*$^{-/-}$ n = 19); lower rheobase currents (Figure 1D; Mann-Whitney; *dSPN* $p = 0.0014$, WT n = 15, SAPAP3 *cKI*$^{-/-}$ n = 21; *iSPN* $p = 0.0024$, WT n = 13, SAPAP3 *cKI*$^{-/-}$ n = 24); and higher input resistances (Figure 1E; Mann-Whitney; *dSPN* $p < 0.0001$, WT n = 15, SAPAP3 *cKI*$^{-/-}$ n = 21; *iSPN* $p = 0.0007$, WT n = 13, SAPAP3 *cKI*$^{-/-}$ n = 21). In addition, dSPNs also exhibited a more depolarized resting membrane potential (Figure 1F; Mann-Whitney; *dSPN* $p = 0.001$, WT n = 16, SAPAP3 *cKI*$^{-/-}$ n = 21; *iSPN* $p = 0.2665$, WT n = 21, SAPAP3 *cKI*$^{-/-}$ n = 27) and decreased capacitance (Figure 1G; Mann-Whitney; *dSPN* $p = 0.0392$, WT n = 15, SAPAP3 *cKI*$^{-/-}$ n = 20; *iSPN* $p = 0.1047$, WT n = 9, SAPAP3 *cKI*$^{-/-}$ n = 20), adding a layer of pathway specificity to the observed changes in somatic excitability. Along with capacitance, somatic area and total dendritic length were selectively reduced in dSPNs (Figure S2), suggesting that anatomical alterations may contribute to the increased excitability of SPNs in the direct pathway. Altogether, these changes are consistent with increased SPN firing rates as described above and observed in SAPAP3 KOs *in vivo*.[27]

While deletion of SAPAP3 increased the excitability of SPN soma, it is their dendrites that contain the SAPAP3-enriched postsynaptic densities that are targeted by corticostriatal synapses[20,30] and directly shape synaptic integration.[41–43] We measured the degradation of backpropagating action potential (bAP)-evoked local Ca^{2+} transients, from proximal to distal dendrites, as a surrogate marker of dendritic excitability in SAPAP3 *cKI*$^{-/-}$ mice[44,45] (Figure 2A). bAP-evoked Ca^{2+} transients were significantly larger in the distal dendrites of dSPNs in SAPAP3 *cKI*$^{-/-}$ mice, suggesting enhanced dendritic excitability (Figures 2B

and 2C; Mann-Whitney; p = 0.021, WT n = 31, SAPAP3 *cKI*$^{-/-}$ n = 31). The dendritic excitability of iSPNs, however, was unaltered (Figures 2B and 2C; Mann-Whitney; p = 0.7424, WT n = 30, SAPAP3 *cKI*$^{-/-}$ n = 32). This pathological enhancement of dSPN dendritic excitability (and lack of change in iSPNs) was also observed in response to sustained bursts of bAPs mimicking ongoing activity (Figures 2D and 2E; Mann-Whitney; *dSPN* p = 0.0036, WT n = 34, SAPAP3 *cKI*$^{-/-}$ n = 42; *iSPN* p = 0.7488, WT n = 29, SAPAP3 *cKI*$^{-/-}$ n = 39). Thus, constitutive deletion of SAPAP3 triggers pathway-specific adaptations in the anatomy and intrinsic excitability of SPNs that are consistent with biased striatal output toward the direct pathway.

Constitutive deletion of SAPAP3 generates a hypercholinergic state in the dorsal striatum

While striatal output is driven by synaptic inputs to SPNs, it is profoundly shaped by non-synaptic processes such as the intrinsic excitabilities of SPNs (above) and intrastriatal release of neuromodulators.[8,9] Among the most influential of these neuromodulators are monoamines (such as dopamine and serotonin) and ACh. There is evidence for abnormal monoaminergic signaling in both patients with OCD and animal models of OCD,[3,17,46,47] and experimental manipulation of striatal Ach can promote tic- and OCD-like behavioral stereotypies in rodents.[48–50] While the sources of monoamines are extrastriatal, the predominant source of striatal ACh is from CINs residing within the striatum itself.[8,9,51] Furthermore, like SPNs, CINs robustly express SAPAP3.[52] We therefore investigated the impact of constitutive SAPAP3 deletion on striatal cholinergic signaling. Choline acetyltransferase (ChAT) immunohistochemistry was performed to visualize and quantify striatal CIN soma density in the precommissural striatum of WT and symptomatic SAPAP3 *cKI*$^{-/-}$ mice (Figure 3). Strikingly, we found that the density of striatal ChAT-positive soma was increased in SAPAP3 *cKI*$^{-/-}$ mice (Figures 3A and 3B; Mann-Whitney; p = 0.0048; WT N = 10, SAPAP3 cKI$^{-/-}$ N = 11). The increase in CIN density was restricted to the dorsal striatum (Figure 3B; Figure S3A; Mann-Whitney; dorsal p = 0.0021; WT N = 10, SAPAP3 *cKI*$^{-/-}$ N = 11) and displayed a slight caudal to rostral gradient (Figure 3C; mixed-effects analysis; p = 0.0033, F(1,19) = 11.27; WT N = 10, SAPAP3 *cKI*$^{-/-}$ N = 11).

Does the increase in CIN density in SAPAP3 *cKI*$^{-/-}$ mice translate functionally to an increase in ACh release? To test this, we infected the dorsal striatum with the genetically encoded ACh sensor $GRAB_{ACh3.0}$ (ACh3.0)[53] and used 2-photon laser scanning microscopy (2PLSM) to measure electrically evoked ACh release in acute brain slices (Figure 3D). Electrically evoked ACh3.0 fluorescence signals were significantly larger in SAPAP3 *cKI*$^{-/-}$ mice across a large range of stimulus intensities (Figures 3E and 3F; Mann-Whitney; 0.01 mA p = 0.1716, 0.05 mA p = 0.0067, 0.1 mA p = 0.0019, 0.2 mA p = 0.0048, 0.3 mA p = 0.0017; WT n = 17, 2 mice, SAPAP3 *cKI*$^{-/-}$ n = 19, 3 mice). Specificity of the fluorescence signal as an indicator of sensor-ACh binding was confirmed using the muscarinic ACh receptor antagonist scopolamine hydrobromide (10 μM) (Figures S3B and S3C). In addition to enhanced evoked ACh release, basal firing rates of CINs were also elevated in SAPAP3 *cKI*$^{-/-}$ mice, as revealed by cell-attached recordings (Figures 3G and 3H; Mann-Whitney; p = 0.0103; WT n = 28, SAPAP3 *cKI*$^{-/-}$ n = 20).

Constitutive deletion of SAPAP3 attenuates cholinergic signaling in striatal SPNs

Although striatal levels of ACh may be higher in SAPAP3 *cKI*$^{-/-}$ mice, it is not clear how SPNs perceive such an increase. SPNs express type 1 and 4 muscarinic receptors (M1 and M4, respectively) but not nicotinic receptors.[54–56] Muscarinic receptors modulate a constellation of conductances that ultimately regulate SPN somatic and dendritic excitability.[45,55,57,58] Importantly, while both dSPNs and iSPNs express M1 receptors, dSPNs also abundantly express M4 receptors: the unique linkage of M1 and M4 receptors to Gα and Gi/o G proteins, respectively, sets the stage for pathway-specific (and opposing) cholinergic modulation of SPNs.[45,55,56,59] While a global increase in muscarinic signaling itself would not readily explain the dSPN-specific enhancement in dendritic excitability described above, alterations in the responses to ongoing ACh release via muscarinic receptors may provide further insight. We therefore measured SPN dendritic excitability in ex vivo brain slices from WT and SAPAP3 *cKI*$^{-/-}$ mice before and after bath application of the muscarinic antagonist atropine (10 μM). Atropine reduced dendritic excitability in both dSPNs and iSPNs from WT mice but not SAPAP3 *cKI*$^{-/-}$ mice (Figures 4A and 4B; pre- vs. postatropine: Wilcoxon matched pairs; WT dSPN p = 0.0305, n = 17, SAPAP3 *cKI*$^{-/-}$ dSPN p = 0.2734, n = 13, WT iSPN p = 0.0105, n = 13, SAPAP3 *cKI*$^{-/-}$ iSPN p = 0.2069, n = 17; WT vs. SAPAP3 *cKI*$^{-/-}$: Mann-Whitney; dSPN p = 0.016, iSPN p = 0.0512).

In the above experiments, dendritic excitability was estimated from the relative decrement of bAP-evoked Ca^{2+} transients measured along SPN dendritic shafts. In addition to somatic excitability and bAP propagation, muscarinic receptors modulate local Ca^{2+} influx and mobilization from intracellular stores.[60–63] We therefore measured the modulatory effect of atropine on evoked Ca^{2+} transients within SPN distal dendritic spines, as an additional readout of muscarinic signaling. Atropine significantly reduced spinous Ca^{2+} transients evoked by bursts of bAPs in both dSPNs and iSPNs from WT mice. This modulation, however, was significantly attenuated in SPNs from SAPAP3 *cKI*$^{-/-}$ mice (Figures 4C–4E; pre- vs. postatropine: Wilcoxon matched pairs; WT dSPN p = 0.0208, n = 18, SAPAP3 *cKI*$^{-/-}$ dSPN p > 0.9999, n = 15, WT iSPN p = 0.0002, n = 14, SAPAP3 *cKI*$^{-/-}$ iSPN p = 0.0001, n = 20; WT vs. SAPAP3 *cKI*$^{-/-}$: Mann-Whitney; dSPN p = 0.3376, iSPN p = 0.0009). While muscarinic signaling was reduced in both SPN types in SAPAP3 *cKI*$^{-/-}$ mice, this occurred in different ways. In iSPNs, the overall percentage of change in Ca^{2+} transients induced by atropine was reduced across the population of measured spines in the mutants. In dSPNs, however, the proportion of spines in which atropine increased vs. decreased Ca^{2+} transients was enlarged (Figures 4E and 4F; Fisher's exact; *dSPN* p = 0.0332, WT n = 31 spines, SAPAP3 *cKI*$^{-/-}$ n = 24 spines; *iSPN* p = 0.7238, WT n = 22 spines, SAPAP3 *cKI*$^{-/-}$ n = 35 spines). Further analysis of the atropine-sensitive component of spine Ca^{2+} transients revealed an activity-dependent aspect of muscarinic modulation: both normal muscarinic signaling and impairment of muscarinic signaling in SAPAP3 *cKI*$^{-/-}$ mice become more prominent as spiking activity continues (Figure 4G; Mann-Whitney; *dSPN* WT n = 18, SAPAP3 *cKI*$^{-/-}$ n = 16; *iSPN* WT n = 14, SAPAP3 *cKI*$^{-/-}$ n = 20), suggesting that deletion of SAPAP3 may impair the striatum's ability to effectively modulate extended bouts of striatal activity.

While SPNs exclusively express M4 and/or M1 muscarinic receptors, the striatum is richly endowed with other types of ACh receptors as well, many of which are located on presynaptic corticostriatal axon terminals. For example, activation of presynaptic M2 muscarinic receptors or α7-containing nicotinic ACh receptors (nAChRs) can reduce or augment corticostriatal glutamate release, respectively.[54,55] Blockade of muscarinic receptors with atropine (10 μM) increased both the amplitude of evoked excitatory postsynaptic currents (EPSCs) and the frequency of spontaneous EPSCs (sEPSCs) measured in SPNs in SAPAP3 *cKI*$^{-/-}$ mice but not WT mice; blockade of nAChRs with mecamylamine (10 μM) had no effect on evoked EPSC amplitude or sEPSC frequency in either WT (consistent with previous reports[64]) or SAPAP3 *cKI*$^{-/-}$ mice (Figure S4). This suggests that not only is signaling through presynaptic muscarinic receptors on glutamatergic afferents intact, but tonic muscarinic suppression of synaptic glutamate release is unmasked in mutant mice, likely a consequence of elevated CIN firing and ACh release described above. Unlike presynaptic muscarinic modulation, presynaptic nicotinic modulation of glutamate release is not augmented or unmasked under basal conditions in SAPAP3 *cKI*$^{-/-}$ mice, suggesting that the net presynaptic effect of elevated basal ACh on glutamatergic synaptic release in mutants is inhibitory.

Basal modulation of SPNs by endogenously released ACh is attenuated in SAPAP3 *cKI*$^{-/-}$ mice; if this impairment is due to diminished muscarinic receptor function, then responses to an exogenous muscarinic receptor agonist should also be attenuated. To address this question, we examined how the muscarinic receptor agonist muscarine (3 μM) modulates AP-evoked dendritic Ca^{2+} transients. Similar to atropine, the effects of muscarine were attenuated in both dSPNs and iSPNs of SAPAP3 *cKI*$^{-/-}$ mice (Figures 4H and 4I; H: pre- vs. postmuscarine: Wilcoxon matched pairs; WT dSPN $p < 0.0001$, n = 21, SAPAP3 *cKI*$^{-/-}$ dSPN $p = 0.3642$, n = 20; WT iSPN $p = 0.0060$, n = 21, SAPAP3 *cKI*$^{-/-}$ $p = 0.1722$, n = 21). Notably, dSPNs and iSPNs responded to muscarine in opposite ways (muscarine reduced Ca^{2+} transients in WT dSPNs and increased them in iSPNs), a finding consistent with the pathway-specific expression patterns of M1 and M4 muscarinic receptors.[56,59] As with atropine, both the effects of muscarine in WT mice and the impairment in muscarinic modulation of Ca^{2+} transients in SAPAP3 *cKI*$^{-/-}$ mice become more prominent as spiking continues (Figure 4J; Mann-Whitney; *dSPN* WT n = 21, SAPAP3 *cKI*$^{-/-}$ n = 19; *iSPN* WT n = 17, SAPAP3 *cKI*$^{-/-}$ n = 25).

DISCUSSION

This study reveals that deletion of the OCD-associated synaptic gene SAPAP3, which causes corticostriatal synaptic dysfunctions and compulsive overgrooming, results in broad alterations in striatal neuronal excitability and neuromodulation. This includes a general increase in SPN somatic excitability, pathway-specific augmentation of dSPN dendritic excitability, hypercholinergic tone, and impaired muscarinic signaling. Together, these data describe how manipulation of a single postsynaptic risk gene can lead to widespread alterations in intrinsic striatal function that will, ultimately, change the landscape upon which impaired corticostriatal synapses act. It also highlights the role of the cholinergic system as a potential target for therapeutic intervention in OCD.

We restricted our study to the dorsolateral striatum for several reasons: (1) it has been proposed that compulsions may represent exaggerated habits,[2,5] (2) habit learning is dysregulated in SAPAP3 KO mice,[65,66] (3) habit learning has been linked to activity in the dorsolateral striatum of mice,[34–38,67,68] and (4) corticostriatal synapses within the dorsolateral striatum are impaired in SAPAP3 KO mice.[20,26,30] Unlike the central "associative" striatum of SAPAP3 KO mice (which also displays corticostriatal synaptic impairments),[28] we found that somatic excitability is elevated in both dSPNs and iSPNs in the dorsolateral striatum. This is consistent with observations that baseline firing rates of SPNs are increased in the striatum of SAPAP3 KOs[27,69] and that striatal activity is elevated in patients with OCD.[6] In contrast to somatic excitability, dendritic excitability was exclusively enhanced in dSPNs. As all cortical inputs to SPNs target dendrites,[8] and as dendritic excitability profoundly shapes how SPNs respond to convergent corticostriatal inputs,[42,70] this pathway-specific augmentation of dendritic excitability could help explain how cortically evoked synaptic activity is biased toward the direct pathway in SAPAP3 KO mice.[31]

Why does deletion of a synaptic gene cause cell-wide changes in excitability? One possibility is that the changes in excitability represent homeostatic adaptations to impaired excitatory drive.[71] Another (non-mutually exclusive) possibility is that normal neuromodulatory processes are altered. ACh, via muscarinic receptors, modulates K^+ and voltage-gated Ca^{2+} channels that regulate SPN somatic and dendritic excitability.[55,61] Though acute blockade of muscarinic receptors did not normalize dSPN dendritic excitability in SAPAP3 *cKO*$^{-/-}$ mice, pathway-specific adaptations to chronically attenuated muscarinic signaling would be consistent with the opposing effects of ACh on dSPN and iSPN excitability. While pathological dopamine signaling has been observed in patients with OCD and mouse models of OCD,[3,17,46,47] the fact that dendritic excitability was unchanged in D2-dopamine-receptor-expressing iSPNs, which are exquisitely sensitive to changes in dopaminergic signaling, makes altered dopaminergic modulation an unlikely culprit in this instance.[45,71] One other possibility is that changes in excitability may involve pathologically elevated mGluR5 signaling.[25,26] Indeed, mGluR5 receptors can modulate somatic excitability and SPN dendritic Ca^{2+} signaling,[43,72] and blockade of mGluR5 receptors normalizes imbalanced cortically driven striatal output in SAPAP3 KO mice.[31] It is unclear how elevated mGluR5 signaling might lead to pathway-specific changes in dendritic excitability though, given that both dSPNs and iSPNs are hyper-responsive to mGluR5 activation in SAPAP3 KO mice.[25,26]

Strikingly, constitutive deletion of SAPAP3 led to an increase in dorsal striatum CIN density and evoked ACh release. This is intriguing in light of two lines of evidence. First, recent studies have discovered that children with pediatric autoimmune neuropsychiatric disorder associated with streptococcus (PANDAS), a condition associated with early-onset OCD symptoms, exhibit immunoglobulin G (IgG) antibodies that bind to and decrease the activity of CINs.[73,74] Second, both ablation of striatal CINs and augmentation of striatal ACh release (by overexpression of the vesicular ACh transporter) accentuate stress- and/or psychostimulant-evoked stereotypies in mice, with CIN ablation leading to tic-like stereotypies or extending cocaine-induced stereotypies and elevated ACh release exacerbating psychostimulant-induced stereotypies.[48–50] Why would both elevations and

presumed decreases in striatal ACh release enhance behavioral stereotypies? One possibility is that there is simply an optimal level of ACh release for normal striatal function, with deviations too far above or below leading to pathological behavior. But the answer may be more nuanced, as implied by our observations of both hyper- and hypo-cholinergic pathologies in SAPAP3 *cKI*$^{-/-}$ mice: while evoked ACh release is elevated, signaling through muscarinic receptors is attenuated in SPNs. Thus, the complex and paradoxical consequences of CIN dysfunction on repetitive behaviors are likely due to the rich milieu of muscarinic (and nicotinic) AChRs located throughout the striatum. While muscarinic signaling in SPNs is impaired, other receptors (or downstream signaling arms of the same receptors) may track changes in ACh very differently.[54,55,75] Indeed, the muscarinic receptors controlling glutamatergic synaptic release do not appear to be impaired, resulting in enhanced basal cholinergic suppression of glutamatergic synaptic transmission in SAPAP3 null mice.

Taken together, the alterations in SPN excitability and cholinergic signaling described here suggest a scenario where pathological ACh release may exacerbate previously described corticostriatal synaptic deficits[20,25,26,28,29] by attenuating presynaptic glutamate release, while impaired postsynaptic muscarinic signaling and cell-type-specific changes in dendritic excitability would bias the striatal response to these inputs toward the direct pathway.

Limitations of the study

This study describes opposing alterations in cholinergic signaling in the SAPAP3 *cKI*$^{-/-}$ mouse model of OCD: (1) increased striatal CIN density and evoked ACh release and (2) decreased basal ACh signaling through muscarinic receptors on SPNs. How striatal CIN density is enhanced is not clear, though we note that CINs are not the only class of striatal interneurons whose numbers are impacted by deletion of SAPAP3.[27] While CINs are the major source of ACh in the dorsal striatum, and they are even more abundant after the loss of SAPAP3, they are not the only source. It remains to be determined if ACh release from other sources, such as the pedunculopontine nucleus,[76] is augmented as well. We also note that this study focused on functional alterations in the dorsolateral striatum, for reasons outlined above. Counterintuitively, optogenetic inhibition of iSPNs (but not dSPNs) in the dorsomedial striatum has been shown to decrease grooming events in Sapap3 KO mice,[32] a likely reflection of the regional diversity of the striatum in shaping complex behaviors.[34–38,67] Finally, the focus of this study is on the basal changes in excitability and modulation of SPNs that emerge in a mouse model of OCD. While basal muscarinic signaling in SPNs is attenuated and spontaneous CIN firing rates are elevated in SAPAP3 *cKI*$^{-/-}$ mice, limitations in ACh sensor sensitivity under our experimental conditions preclude the ability to accurately estimate basal levels of ACh in *ex vivo* brain slices from WT and mutant mice.

STAR★METHODS

Detailed methods are provided in the online version of this paper and include the following:

RESOURCE AVAILABILITY

Lead contact—Further information and requests for resources and reagents may be directed to and will be fulfilled by Lead Contact, Joshua L. Plotkin, Ph.D., (joshua.plotkin@stonybrook.edu).

Materials availability—Mouse lines generated in this study will be made available upon request.

Data and code availability

- Detailed datasets supporting the current study are available from the corresponding author upon request.
- This paper does not report any original code.
- Any additional information required to reanalyze the data reported in this paper is available from the lead contact upon request.

EXPERIMENTAL MODEL AND SUBJECT DETAILS

Animal subjects—All experimental procedures were performed in accordance with the United States Public Health Service *Guide for Care and Use of Laboratory Animals* (Institute of Laboratory Animal Resources, National Research Council), and were approved by the Institutional Animal Care and Use Committee at Stony Brook University. Animals were housed 2–5 per cage in an environmentally controlled room (20°C–23°C, 30–70% humidity, 12h light/dark cycles) with food and water available *ad libitum*, and cages were cleaned once per week. Due to tendency of mutant animals to develop facial and bodily lesions, enhanced animal welfare care was deemed necessary and topical treatments with triple antibiotic ointment were administered by veterinary staff as needed. All experiments were performed in 3- to 7-month-old male and female SAPAP3 null mice (conditional knock-in, generated by Dr. Qiangge Zhang and Dr. Guoping Feng; see Figure S1) or their WT controls, crossed with 1 of 3 BAC transgenic lines that express fluorescent reporters either under the D1 (drd1-tdTomato) or D2 (drd2-eGFP) dopamine receptor promoter or ChAT (ChAT-tauGFP) promoter (to target dSPNs, iSPNs and CINs, respectively)[39,40,77]; all mice were on the C57BL/6 background. Experiments performed on SAPAP3$^{-/-}$ mice were carried out after the onset of compulsive grooming and matched alongside wildtype controls of a comparable age.

METHOD DETAILS

Generation of SAPAP3 cKI$^{-/-}$ mice—SAPAP3 conditional knock-in (cKI$^{-/-}$) mice were generated using a similar strategy described previously.[78,79] Specifically, three exons (Ensemble ID: ENSMUSE00001223455, ENSMUSE00000400411, ENSMUSE00000335250) and the introns between those exons of the *Sapap3* gene were inverted and cloned into the FLEX targeting vector.[78] This design allows for Cre-dependent rescue of SAPAP3 expression. Mouse R1 ES cells were used to generate the clones that contain the correct targeting allele. One of those ES clones was implanted into C57 blastocysts to produce the chimeric founder, which was crossed with betaActin-FLP mice

(The Jackson Laboratory, stock#005703) to generate the SAPAP3 cKI$^{-/-}$ mouse line. Those mice were backcrossed to C57BL/6J (The Jackson Laboratory, stock #000664) for >5 generations before use in experiments. In the absence of Cre recombinase, the inverted exons and introns would introduce a reading frameshift and cause degradation of *Sapap3* transcripts. Throughout this study, mice designated as WT were offspring of *Sapap3* heterozygous crosses that contained two unaltered *Sapap3* alleles and mice designated as cKI$^{-/-}$ were offspring that contained two altered *Sapap3* alleles (and hence no SAPAP3 protein). No obvious adverse phenotypes were observed – other than compulsive grooming and elevated anxiety-like behavior – as a result of this breeding scheme (see Figure S1).

Behavioral analyses—For the assessment and quantification of grooming behavior, experimental subjects were habituated to a 13cm diameter acrylic cylinder for 10 min daily, 3 days prior to video acquisition (10 min on the fourth day). Grooming behavior was manually analyzed based on Welch et al. 2007,[20] to confirm overgrooming in SAPAP3 cKI$^{-/-}$ mice. (see Figure S1). Open field measurements were carried out in a 43 cm^2 arena and video acquisitions were analyzed autonomously using EthoVision XT software (grooming behavior in the open field arena was calculated manually as above, also using EthoVision XT). Behavioral tests were carried out no more than 24 h prior to electrophysiology and imaging experiments.

Ex vivo slice electrophysiology—Acute parasagittal slices (275μm) containing the dorsolateral striatum were obtained from mice following anesthetization with ketamine/xylazine (100 mg/kg/7 mg/kg) and transcardial perfusion with ice-cold artificial cerebral spinal fluid (ACSF) containing (in mM): 124 NaCl, 3 KCl, 1 $CaCl_2$, 1.5 $MgCl_2$, 26 $NaHCO_3$, 1 NaH_2PO_4, and 14 glucose, continuously bubbled with carbogen (95% O_2 and 5% CO_2). Slices were cut using a VT-1000 S vibratome (Leica Microsystems, Buffalo Grove, IL) and transferred to a holding chamber where they were incubated at 32°C for 45 min in ASCF containing (in mM) 2 $CaCl_2$ and 1 $MgCl_2$, after which they were removed and acclimated to room temperature (~21°C) for 15 min before recording. Using a Bruker 2-photon imaging system with integrated electrophysiological capabilities, SPNs were identified via tdTomato or eGFP fluorescence and patch-clamped for whole-cell recordings using electrodes pulled from borosilicate glass (3.5–5MΩ). Current clamp recordings were performed with an internal solution containing (in mM): 135 $KMeSO_4$, 5 KCl, 10 HEPES, 2 ATP-Mg^{2+}, 0.5 GTP-Na^+, 5 phosphocreatine-tris, 5 phosphocreatine-Na^+, 0.1 Fluo-4 pentapotassium salt, and 0.05 Alexa Fluor 568 hydrazide Na^+ salt. Fluo-4 precluded the need for EGTA in Ca^{2+} imaging experiments and Alexa 568 was used to visualize cell bodies, dendrites, and spines. Voltage-clamp recordings were performed with an internal solution containing (in mM): 120 $CsMeSO_3$, 5 NaCl, 10 TEA-Cl (tetraethylammonium-Cl), 10 HEPES, 5 Qx-314, 4 ATP-Mg^{2+}, 0.3 GTP-Na^+, and 0.25 EGTA. Electrophysiological recordings were digitally sampled at 30kHz and filtered at 1kHz using a Multiclamp 700B amplifier (Molecular Devices, San Jose, CA). Input resistance and membrane capacitance were measured in voltage-clamp mode (V_{hold} = −70mV) from single 20ms, 5mV depolarizing steps. Current-voltage (IV) curves, induced firing frequencies and rheobase measures were made in current-clamp mode while injecting minimal current (0–75pA) to maintain all SPNs at equivalent membrane potentials (~−81 mV), since group differences

in V_{rest} were observed. Cell attached recordings from CINs were performed in voltage clamp mode to quantify baseline firing rates. sEPSCs were recorded in voltage-clamp mode (V_{hold} = −70mV) for 180s before and after bath applying drug. Local electrical stimulation was evoked using a concentric bipolar stimulation electrode (FHC, Inc., Bowdoin, ME) at an amplitude of 1–3mV (tuned to evoke EPSCs ~100pA). EPSCs were averaged from 10 sweeps, each separated by 10s; sweeps included 2 pulses (20Hz); all data presented were obtained from the first pulse. CIN firing rates, electrical stimulation and sEPSC experiments were performed at 26°C–29°C; all other experiments were performed at 21±°C.

2-Photon Ca^{2+} laser scanning microscopy, Ca^{2+} imaging and ACh sensor measurements—dSPNs and iSPNs were identified via somatic tdTomato and enhanced-GFP 2-photon excited fluorescence using an Ultima Laser Scanning Microscope System (Bruker Nano, Inc., Middleton, WI) equipped with an Olympus 60X/1.0 water-dipping lens (Olympus, Center Valley, PA). For simultaneous electrophysiological and 2-photon Ca^{2+} imaging experiments, green and red fluorescent signals were obtained using 810nm pulsed light excitation (90MHz) (Chameleon Ultra II, Coherent, Inc., Santa Clara, CA) and top-mounted external detectors with 607/45 nm and 525/70 nm emission filters (Hamamatsu Corp., Bridgewater, NJ). Patched SPNs were allowed to equilibrate to the internal recording solution prior to any experimental imaging for a minimum of 15 min after patch rupture to ensure adequate filling of distal dendrites. *Ca^{2+} imaging*: Dendritic Ca^{2+} transients were measured using Fluo-4.[45] Line scans of green (G) and red (R) fluorescence were acquired at proximal (45μm–60μm) and distal (90μm–130μm) adjacent dendritic spines and shafts at 5.342ms and 512 pixels per line with 0.0776μm^2 pixels at 10μs dwell. Ca^{2+} transients were expressed as ΔG/R, and dendritic indexes were quantified as distal Ca^{2+} transient area (ΔG/R•ms) divided by the largest proximal Ca^{2+} transient area (for single bAPs) or the average of 2–5 proximal Ca^{2+} transient areas (for bAP bursts), all acquired from dendritic shafts.[44] Single bAPs were generated by a somatic current injection (2nA, 2ms) and bursts of bAPs were delivered at 5Hz, each burst containing 3 bAPs at 50Hz (20ms interval).[43] Line scans began 300ms before stimuli and continued for 698ms (for single bAPs) or 1670ms (for bAP theta bursts) after the stimuli ended. All drugs were dissolving in the external ACSF and bath applied for a minimum of 10 min prior to comparative experimentation. *ACh sensor measurements*: To evoke ACh release, a concentric stimulating electrode (FHC) powered by an ISO-Flex Stimulus Isolator (Microprobes for Life Science) was centered on the y-plane and placed just outside of the objective field. Spiral line scans (920nm, 21.2ms with 0.0776μm^2 pixels and 10μs dwell) were placed over infected neuropil and acquired sequentially, at least 5 s apart, while delivering single 1ms electrical stimuli of increasing intensities. Line scans began 1000ms before stimuli and continued for 4000ms after the stimuli ended.

Surgical procedures—All mice subjected to surgical procedures were induced and maintained under anesthesia via inhalation of vaporized isoflurane (3% for induction and 1%–2% for maintenance during surgery) and administered a post-operative analgesic, Meloxicam (5 mg/kg), via subcutaneous injection as needed. Prior to any surgical procedure, complete sedation was confirmed via tail pinch, animals were placed in a stereotaxic apparatus, the scalp was shaved and disinfected, and eyes were covered with

an eye-protective gel (Puralube Ophthalmic Ointment, Dechra Veterinary Products). A 1μL Hamilton Neuros micro-volume syringe was used for unilateral dorsolateral striatum injections (−2.20 mm ML, 0.62mm AP, −2.80mm DV) and manipulated via a motorized stereotaxic injector (Quintessential Stereotaxic Injector QSI, Stoelting Co.) controlled by Angle Two software (Leica Biosystems). 200nL of AAV5-hSyn-ACh3.0(ACh.4.3) (ACh3.0; titer: $\geq 1 \cdot 10^{13}$vg/ml)[53] were injected over 5 min and a further 5 min was allowed for diffusion before slowly withdrawing the needle. All subjects were monitored daily for pain for 72h and sacrificed for experimentation after a postoperative period of 3–4 weeks.

Immunohistochemistry—Experimental subjects were anesthetized by isoflurane inhalation before transcardial perfusion with PBS, then 4% paraformaldehyde (PFA) (Electron Microscopy Sciences) before brain extraction (note that all IHC dilutions are in 1x phosphate-buffered saline [PBS]). Extracted brains were fixed in 4% PFA for a further 12 h at 4°C, then cryopreserved with 30% sucrose in 1x PBS for 48 h at 4°C. Fixed brain tissue was frozen in O.C.T. (Fisher) and sliced coronally at 50μm thickness using a cryostat (Leica). For antibody labeling, brain slices were blocked for 2h at room temperature (3% normal donkey serum [Sigma D9663], 0.1% Triton X-), stained with primary antibody for 12 h at 4°C (EMD Millipore [ab144P, RRID: AB_2079751] goat anti-ChAT, 1:500 dilution), washed 3 × 10 min (0.5% NDS, 0.1% Triton X-), stained with secondary antibody for 2 h at room temperature (Abcam [ab150132, RRID: AB_2810222] donkey anti-goat Alexa Fluor 594, 1:2000 concentration), then washed 3 × 10 min as above before placing in PBS and mounting onto microscope slides with Fluoromount-G (SouthernBiotech). Another antibody combination was used alongside ChAT labeling (rabbit anti-μOR [Abcam [ab10275, RRID: AB_2156356]] and donkey anti-rabbit 488 [Invitrogen [A-21206, RRID: AB_2535792]]), but not analyzed as part of this study. Coronal sections were collected from the pre-commissural striatum and binned at 200μm increments (1.25mm–1.05mm to 0.45mm–0.25mm bregma).

Immunohistochemistry image acquisition & analysis—Images were obtained using a VS.120-S6-W virtual slide microscope (Olympus) at 20x magnification. Images were composed of 30 1μm z-planes. Image analysis was performed by two blinded investigators using ImageJ[80] (Fiji [RRID: SCR_002285]). The 15 most in-focus planes in the z-stacks were max-projected and thresholded. Semi-automated quantification of ChAT-positive cell bodies was performed using ImageJ's[80] Particle Analysis function. Identified cells were manually checked for accuracy. Striatal regions were manually outlined using the lateral ventricles, callosum, and a straight line from the inferior ventricular apex to the inferomedial corner of the piriform cortex to reproducibly demarcate the striatum. Dorsal and ventral striatal domains were established by a horizontal partition dividing the entire striatum into two equal areas.

SPN dendritic anatomy analysis—Sholl analyses were performed on z-stacks of Alexa Fluor 568-filled SPNs resliced to the appropriate voxel length; dendritic arbors were manually traced using neuTube[81] and individually processed in ImageJ[80] Simple Neurite Tracer's Sholl analysis function.

QUANTIFICATION AND STATISTICAL ANALYSES

Electrophysiological recordings and Ca^{2+} transients were analyzed using Igor Pro (WaveMetrics, Inc., Lake Oswego, OR [RRID: SCR_000325]). Statistical differences were examined using 2-sided Mann-Whitney U, Wilcoxon signed-rank (for paired comparisons), two-way ANOVA (for grouped comparisons) followed by Bonferroni's multiple comparisons test, or Fisher's exact tests. Differences were considered to be statistically significant if $p < 0.05$. All statistical tests were performed in GraphPad Prism v10 (GraphPad Software, La Jolla, CA [RRID: SCR_002798]) following a Grubb's test for outliers (alpha = 0.05), also in Prism. Typically no more than 1 outlier was identified and removed from any given dataset, with a maximum of 2 outliers identified and removed in rare instances. The Shapiro-Wilk test for normality was used to confirm the appropriateness of parametric statistics. Boxplots were generated in Prism using the Tukey method. All statistical details can be found in the Results section as well as in the figure legends.

Supplementary Material

Refer to Web version on PubMed Central for supplementary material.

ACKNOWLEDGMENTS

We thank W. Akmentin for technical support. This study was supported by NIH NINDS R01 NS104089 to J.L.P. Portions of the graphical abstract were created with BioRender.com.

REFERENCES

1. Ahmari SE, and Dougherty DD (2015). DISSECTING OCD CIRCUITS: FROM ANIMAL MODELS TO TARGETED TREATMENTS. Depress. Anxiety 32, 550–562. 10.1002/da.22367. [PubMed: 25952989]
2. Graybiel AM, and Rauch SL (2000). Toward a neurobiology of obsessive-compulsive disorder. Neuron 28, 343–347. 10.1016/s0896-6273(00)00113-6. [PubMed: 11144344]
3. Pauls DL, Abramovitch A, Rauch SL, and Geller DA (2014). Obsessive-compulsive disorder: an integrative genetic and neurobiological perspective. Nat. Rev. Neurosci. 15, 410–424. 10.1038/nrn3746. [PubMed: 24840803]
4. Ting JT, and Feng G (2011). Neurobiology of obsessive-compulsive disorder: insights into neural circuitry dysfunction through mouse genetics. Curr. Opin. Neurobiol. 21, 842–848. 10.1016/j.conb.2011.04.010. [PubMed: 21605970]
5. Burguière E, Monteiro P, Mallet L, Feng G, and Graybiel AM (2015). Striatal circuits, habits, and implications for obsessive-compulsive disorder. Curr. Opin. Neurobiol. 30, 59–65. 10.1016/j.conb.2014.08.008. [PubMed: 25241072]
6. Saxena S, Brody AL, Schwartz JM, and Baxter LR (1998). Neuroimaging and frontal-subcortical circuitry in obsessive-compulsive disorder. Br. J. Psychiatry 173, 26–37.
7. Wu K, Hanna GL, Rosenberg DR, and Arnold PD (2012). The role of glutamate signaling in the pathogenesis and treatment of obsessive-compulsive disorder. Pharmacol. Biochem. Behav. 100, 726–735. 10.1016/j.pbb.2011.10.007. [PubMed: 22024159]
8. Gerfen CR, and Surmeier DJ (2011). Modulation of striatal projection systems by dopamine. Annu. Rev. Neurosci. 34, 441–466. 10.1146/annurev-neuro-061010-113641. [PubMed: 21469956]
9. Plotkin JL, and Goldberg JA (2019). Thinking Outside the Box (and Arrow): Current Themes in Striatal Dysfunction in Movement Disorders. Neuroscientist 25, 359–379. 10.1177/1073858418807887. [PubMed: 30379121]

10. van Maanen L, Fontanesi L, Hawkins GE, and Forstmann BU (2016). Striatal activation reflects urgency in perceptual decision making. Neuroimage 139, 294–303. 10.1016/j.neuroimage.2016.06.045. [PubMed: 27355435]
11. Cui G, Jun SB, Jin X, Pham MD, Vogel SS, Lovinger DM, and Costa RM (2013). Concurrent activation of striatal direct and indirect pathways during action initiation. Nature 494, 238–242. 10.1038/nature11846. [PubMed: 23354054]
12. Kravitz AV, Freeze BS, Parker PRL, Kay K, Thwin MT, Deisseroth K, and Kreitzer AC (2010). Regulation of parkinsonian motor behaviours by optogenetic control of basal ganglia circuitry. Nature 466, 622–626. 10.1038/nature09159. [PubMed: 20613723]
13. Pittenger C, Kelmendi B, Bloch M, Krystal JH, and Coric V (2005). Clinical treatment of obsessive compulsive disorder. Psychiatry 2, 34–43.
14. Pittenger C (2015). Glutamatergic agents for OCD and related disorders. Curr. Treat. Options Psychiatry 2, 271–283. 10.1007/s40501-015-0051-8. [PubMed: 26301176]
15. Pittenger C, and Bloch MH (2014). Pharmacological treatment of obsessive-compulsive disorder. Psychiatr. Clin. 37, 375–391. 10.1016/j.psc.2014.05.006.
16. Rosenberg DR, Mirza Y, Russell A, Tang J, Smith JM, Banerjee SP, Bhandari R, Rose M, Ivey J, Boyd C, and Moore GJ (2004). Reduced anterior cingulate glutamatergic concentrations in childhood OCD and major depression versus healthy controls. J. Am. Acad. Child Adolesc. Psychiatry 43, 1146–1153. 10.1097/01.chi.0000132812.44664.2d. [PubMed: 15322418]
17. Bellini S, Fleming KE, De M, McCauley JP, Petroccione MA, D'Brant LY, Tkachenko A, Kwon S, Jones LA, and Scimemi A (2018). Neuronal Glutamate Transporters Control Dopaminergic Signaling and Compulsive Behaviors. J. Neurosci. 38, 937–961. 10.1523/jneurosci.1906-17.2017. [PubMed: 29229708]
18. International Obsessive Compulsive Disorder Foundation Genetics Collaborative IOCDF-GC and OCD Collaborative Genetics Association Studies OCGAS (2018). Revealing the complex genetic architecture of obsessive-compulsive disorder using meta-analysis. Mol. Psychiatr. 23, 1181–1188. 10.1038/mp.2017.154.
19. Shmelkov SV, Hormigo A, Jing D, Proenca CC, Bath KG, Milde T, Shmelkov E, Kushner JS, Baljevic M, Dincheva I, et al. (2010). Slitrk5 deficiency impairs corticostriatal circuitry and leads to obsessive-compulsive-like behaviors in mice. Nat. Med. 16, 598–602, 1p following 602, 591p following 602. 10.1038/nm.2125. [PubMed: 20418887]
20. Welch JM, Lu J, Rodriguiz RM, Trotta NC, Peca J, Ding JD, Feliciano C, Chen M, Adams JP, Luo J, et al. (2007). Cortico-striatal synaptic defects and OCD-like behaviours in Sapap3-mutant mice. Nature 448, 894–900. 10.1038/nature06104. [PubMed: 17713528]
21. Kindler S, Rehbein M, Classen B, Richter D, and Böckers TM (2004). Distinct spatiotemporal expression of SAPAP transcripts in the developing rat brain: a novel dendritically localized mRNA. Brain Res. Mol. Brain Res. 126, 14–21. 10.1016/j.molbrainres.2004.03.014. [PubMed: 15207911]
22. Rajendram R, Kronenberg S, Burton CL, and Arnold PD (2017). Glutamate Genetics in Obsessive-Compulsive Disorder: A Review. J Can Acad Child Adolesc Psychiatry 26, 205–213. [PubMed: 29056983]
23. Welch JM, Wang D, and Feng G (2004). Differential mRNA expression and protein localization of the SAP90/PSD-95-associated proteins (SAPAPs) in the nervous system of the mouse. J. Comp. Neurol. 472, 24–39. 10.1002/cne.20060. [PubMed: 15024750]
24. Züchner S, Wendland JR, Ashley-Koch AE, Collins AL, Tran-Viet KN, Quinn K, Timpano KC, Cuccaro ML, Pericak-Vance MA, Steffens DC, et al. (2009). Multiple rare SAPAP3 missense variants in trichotillomania and OCD. Mol. Psychiatr. 14, 6–9. 10.1038/mp.2008.83.
25. Chen M, Wan Y, Ade K, Ting J, Feng G, and Calakos N (2011). Sapap3 deletion anomalously activates short-term endocannabinoid-mediated synaptic plasticity. J. Neurosci. 31, 9563–9573. 10.1523/jneurosci.1701-11.2011. [PubMed: 21715621]
26. Wan Y, Feng G, and Calakos N (2011). Sapap3 deletion causes mGluR5-dependent silencing of AMPAR synapses. J. Neurosci. 31, 16685–16691. 10.1523/jneurosci.2533-11.2011. [PubMed: 22090495]

27. Burguière E, Monteiro P, Feng G, and Graybiel AM (2013). Optogenetic stimulation of lateral orbitofronto-striatal pathway suppresses compulsive behaviors. Science 340, 1243–1246. 10.1126/science.1232380. [PubMed: 23744950]
28. Corbit VL, Manning EE, Gittis AH, and Ahmari SE (2019). Strengthened Inputs from Secondary Motor Cortex to Striatum in a Mouse Model of Compulsive Behavior. J. Neurosci. 39, 2965–2975. 10.1523/jneurosci.1728-18.2018. [PubMed: 30737313]
29. Hadjas LC, Schartner MM, Cand J, Creed MC, Pascoli V, Lüscher C, and Simmler LD (2020). Projection-specific deficits in synaptic transmission in adult Sapap3-knockout mice. Neuropsychopharmacology 45, 2020–2029. 10.1038/s41386-020-0747-3. [PubMed: 32585679]
30. Wan Y, Ade KK, Caffall Z, Ilcim Ozlu M, Eroglu C, Feng G, and Calakos N (2014). Circuit-selective striatal synaptic dysfunction in the Sapap3 knockout mouse model of obsessive-compulsive disorder. Biol. Psychiatr. 75, 623–630. 10.1016/j.biopsych.2013.01.008.
31. Ade KK, Wan Y, Hamann HC, O'Hare JK, Guo W, Quian A, Kumar S, Bhagat S, Rodriguiz RM, Wetsel WC, et al. (2016). Increased Metabotropic Glutamate Receptor 5 Signaling Underlies Obsessive-Compulsive Disorder-like Behavioral and Striatal Circuit Abnormalities in Mice. Biol. Psychiatr. 80, 522–533. 10.1016/j.biopsych.2016.04.023.
32. Ramírez-Armenta KI, Alatriste-León H, Verma-Rodríguez AK, Llanos-Moreno A, Ramírez-Jarquín JO, and Tecuapetla F (2022). Optogenetic inhibition of indirect pathway neurons in the dorsomedial striatum reduces excessive grooming in Sapap3-knockout mice. Neuropsychopharmacology 47, 477–487. 10.1038/s41386-021-01161-9. [PubMed: 34417544]
33. Wang W, Li C, Chen Q, van der Goes MS, Hawrot J, Yao AY, Gao X, Lu C, Zang Y, Zhang Q, et al. (2017). Striatopallidal dysfunction underlies repetitive behavior in Shank3-deficient model of autism. J. Clin. Invest. 127, 1978–1990. 10.1172/jci87997. [PubMed: 28414301]
34. Balleine BW, and O'Doherty JP (2010). Human and rodent homologies in action control: corticostriatal determinants of goal-directed and habitual action. Neuropsychopharmacology 35, 48–69. 10.1038/npp.2009.131. [PubMed: 19776734]
35. Quinn JJ, Pittenger C, Lee AS, Pierson JL, and Taylor JR (2013). Striatum-dependent habits are insensitive to both increases and decreases in reinforcer value in mice. Eur. J. Neurosci. 37, 1012–1021. 10.1111/ejn.12106. [PubMed: 23298231]
36. Yin HH, and Knowlton BJ (2006). The role of the basal ganglia in habit formation. Nat. Rev. Neurosci. 7, 464–476. 10.1038/nrn1919. [PubMed: 16715055]
37. Yin HH, Knowlton BJ, and Balleine BW (2004). Lesions of dorsolateral striatum preserve outcome expectancy but disrupt habit formation in instrumental learning. Eur. J. Neurosci. 19, 181–189. [PubMed: 14750976]
38. O'Hare JK, Ade KK, Sukharnikova T, Van Hooser SD, Palmeri ML, Yin HH, and Calakos N (2016). Pathway-Specific Striatal Substrates for Habitual Behavior. Neuron 89, 472–479. 10.1016/j.neuron.2015.12.032. [PubMed: 26804995]
39. Shuen JA, Chen M, Gloss B, and Calakos N (2008). Drd1a-tdTomato BAC transgenic mice for simultaneous visualization of medium spiny neurons in the direct and indirect pathways of the basal ganglia. J. Neurosci. 28, 2681–2685. 10.1523/jneurosci.5492-07.2008. [PubMed: 18337395]
40. Gong S, Zheng C, Doughty ML, Losos K, Didkovsky N, Schambra UB, Nowak NJ, Joyner A, Leblanc G, Hatten ME, and Heintz N (2003). A gene expression atlas of the central nervous system based on bacterial artificial chromosomes. Nature 425, 917–925. 10.1038/nature02033. [PubMed: 14586460]
41. Carter AG, and Sabatini BL (2004). State-dependent calcium signaling in dendritic spines of striatal medium spiny neurons. Neuron 44, 483–493. 10.1016/j.neuron.2004.10.013. [PubMed: 15504328]
42. Plotkin JL, Day M, and Surmeier DJ (2011). Synaptically driven state transitions in distal dendrites of striatal spiny neurons. Nat. Neurosci. 14, 881–888. 10.1038/nn.2848. [PubMed: 21666674]
43. Plotkin JL, Shen W, Rafalovich I, Sebel LE, Day M, Chan CS, and Surmeier DJ (2013). Regulation of dendritic calcium release in striatal spiny projection neurons. J. Neurophysiol. 110, 2325–2336. 10.1152/jn.00422.2013. [PubMed: 23966676]
44. Carrillo-Reid L, Day M, Xie Z, Melendez AE, Kondapalli J, Plotkin JL, Wokosin DL, Chen Y, Kress GJ, Kaplitt M, et al. (2019). Mutant huntingtin enhances activation of dendritic Kv4 K(+)

channels in striatal spiny projection neurons. Elife 8, e40818. 10.7554/eLife.40818. [PubMed: 31017573]

45. Day M, Wokosin D, Plotkin JL, Tian X, and Surmeier DJ (2008). Differential excitability and modulation of striatal medium spiny neuron dendrites. J. Neurosci. 28, 11603–11614. 10.1523/jneurosci.1840-08.2008. [PubMed: 18987196]
46. Fineberg NA, Chamberlain SR, Hollander E, Boulougouris V, and Robbins TW (2011). Translational approaches to obsessive-compulsive disorder: from animal models to clinical treatment. Br. J. Pharmacol. 164, 1044–1061. 10.1111/j.1476-5381.2011.01422.x. [PubMed: 21486280]
47. Wood J, LaPalombara Z, and Ahmari SE (2018). Monoamine abnormalities in the SAPAP3 knockout model of obsessive-compulsive disorder-related behaviour. Philos. Trans. R. Soc. Lond. B Biol. Sci. 373, 20170023. 10.1098/rstb.2017.0023. [PubMed: 29352023]
48. Aliane V, Pérez S, Bohren Y, Deniau JM, and Kemel ML (2011). Key role of striatal cholinergic interneurons in processes leading to arrest of motor stereotypies. Brain 134, 110–118. 10.1093/brain/awq285. [PubMed: 21097493]
49. Crittenden JR, Lacey CJ, Lee T, Bowden HA, and Graybiel AM(2014). Severe drug-induced repetitive behaviors and striatal overexpression of VAChT in ChAT-ChR2-EYFP BAC transgenic mice. Front. Neural Circ. 8, 57. 10.3389/fncir.2014.00057.
50. Xu M, Kobets A, Du JC, Lennington J, Li L, Banasr M, Duman RS, Vaccarino FM, DiLeone RJ, and Pittenger C (2015). Targeted ablation of cholinergic interneurons in the dorsolateral striatum produces behavioral manifestations of Tourette syndrome. Proc. Natl. Acad. Sci. USA 112, 893–898. 10.1073/pnas.1419533112. [PubMed: 25561540]
51. Zhou FM, Wilson CJ, and Dani JA (2002). Cholinergic interneuron characteristics and nicotinic properties in the striatum. J. Neurobiol. 53, 590–605. 10.1002/neu.10150. [PubMed: 12436423]
52. Saunders A, Macosko EZ, Wysoker A, Goldman M, Krienen FM, de Rivera H, Bien E, Baum M, Bortolin L, Wang S, et al. (2018). Molecular Diversity and Specializations among the Cells of the Adult Mouse Brain. Cell 174, 1015–1030.e16. 10.1016/j.cell.2018.07.028. [PubMed: 30096299]
53. Jing M, Li Y, Zeng J, Huang P, Skirzewski M, Kljakic O, Peng W, Qian T, Tan K, Zou J, et al. (2020). An optimized acetylcholine sensor for monitoring in vivo cholinergic activity. Nat. Methods 17, 1139–1146. 10.1038/s41592-020-0953-2. [PubMed: 32989318]
54. Assous M (2021). Striatal cholinergic transmission. Focus on nicotinic receptors' influence in striatal circuits. Eur. J. Neurosci. 53, 2421–2442. 10.1111/ejn.15135. [PubMed: 33529401]
55. Goldberg JA, Ding JB, and Surmeier DJ (2012). Muscarinic modulation of striatal function and circuitry. Handb. Exp. Pharmacol, 223–241. 10.1007/978-3-642-23274-9_10. [PubMed: 22222701]
56. Shen W, Plotkin JL, Francardo V, Ko WKD, Xie Z, Li Q, Fieblinger T, Wess J, Neubig RR, Lindsley CW, et al. (2015). M4 Muscarinic Receptor Signaling Ameliorates Striatal Plasticity Deficits in Models of L-DOPA-Induced Dyskinesia. Neuron 88, 762–773. 10.1016/j.neuron.2015.10.039. [PubMed: 26590347]
57. Akins PT, Surmeier DJ, and Kitai ST (1990). Muscarinic modulation of a transient K+ conductance in rat neostriatal neurons. Nature 344, 240–242. 10.1038/344240a0. [PubMed: 2314459]
58. Shen W, Tian X, Day M, Ulrich S, Tkatch T, Nathanson NM, and Surmeier DJ (2007). Cholinergic modulation of Kir2 channels selectively elevates dendritic excitability in striatopallidal neurons. Nat. Neurosci. 10, 1458–1466. 10.1038/nn1972. [PubMed: 17906621]
59. Hersch SM, Gutekunst CA, Rees HD, Heilman CJ, and Levey AI (1994). Distribution of m1-m4 muscarinic receptor proteins in the rat striatum: light and electron microscopic immunocytochemistry using subtype-specific antibodies. J. Neurosci. 14, 3351–3363. 10.1523/jneurosci.14-05-03351.1994. [PubMed: 8182478]
60. Howe AR, and Surmeier DJ (1995). Muscarinic receptors modulate N-P-and L-type Ca2+ currents in rat striatal neurons through parallel pathways. J. Neurosci. 15, 458–469. 10.1523/jneurosci.15-01-00458.1995. [PubMed: 7823150]

61. Oldenburg IA, and Ding JB (2011). Cholinergic modulation of synaptic integration and dendritic excitability in the striatum. Curr. Opin. Neurobiol. 21, 425–432. 10.1016/j.conb.2011.04.004. [PubMed: 21550798]
62. Olson PA, Tkatch T, Hernandez-Lopez S, Ulrich S, Ilijic E, Mugnaini E, Zhang H, Bezprozvanny I, and Surmeier DJ (2005). G-protein-coupled receptor modulation of striatal CaV1.3 L-type Ca2+ channels is dependent on a Shank-binding domain. J. Neurosci. 25, 1050–1062. 10.1523/jneurosci.3327-04.2005. [PubMed: 15689540]
63. Pisani A, Bernardi G, Ding J, and Surmeier DJ (2007). Re-emergence of striatal cholinergic interneurons in movement disorders. Trends Neurosci. 30, 545–553. 10.1016/j.tins.2007.07.008. [PubMed: 17904652]
64. Matityahu L, Malgady JM, Schirelman M, Johansson Y, Wilking JA, Silberberg G, Goldberg JA, and Plotkin JL (2022). A tonic nicotinic brake controls spike timing in striatal spiny projection neurons. Elife 11, e75829. 10.7554/eLife.75829. [PubMed: 35579422]
65. Ehmer I, Feenstra M, Willuhn I, and Denys D (2020). Instrumental learning in a mouse model for obsessive-compulsive disorder: Impaired habit formation in Sapap3 mutants. Neurobiol. Learn. Mem. 168, 107162. 10.1016/j.nlm.2020.107162. [PubMed: 31927083]
66. Hadjas LC, Lüscher C, and Simmler LD (2019). Aberrant habit formation in the Sapap3-knockout mouse model of obsessive-compulsive disorder. Sci. Rep. 9, 12061. 10.1038/s41598-019-48637-9. [PubMed: 31427755]
67. Vicente AM, Galvão-Ferreira P, Tecuapetla F, and Costa RM (2016). Direct and indirect dorsolateral striatum pathways reinforce different action strategies. Curr. Biol. 26, R267–R269. 10.1016/j.cub.2016.02.036. [PubMed: 27046807]
68. Lerner TN (2020). Interfacing behavioral and neural circuit models for habit formation. J. Neurosci. Res. 98, 1031–1045. 10.1002/jnr.24581. [PubMed: 31916623]
69. Mintzopoulos D, Gillis TE, Robertson HR, Dalia T, Feng G, Rauch SL, and Kaufman MJ (2016). Striatal magnetic resonance spectroscopy abnormalities in young adult SAPAP3 knockout mice. Biol. Psychiatry. Cogn. Neurosci. Neuroimaging 1, 39–48. 10.1016/j.bpsc.2015.10.001. [PubMed: 26858992]
70. Prager EM, Dorman DB, Hobel ZB, Malgady JM, Blackwell KT, and Plotkin JL (2020). Dopamine Oppositely Modulates State Transitions in Striosome and Matrix Direct Pathway Striatal Spiny Neurons. Neuron 108, 1091–1102.e5. 10.1016/j.neuron.2020.09.028. [PubMed: 33080228]
71. Fieblinger T, Graves SM, Sebel LE, Alcacer C, Plotkin JL, Gertler TS, Chan CS, Heiman M, Greengard P, Cenci MA, and Surmeier DJ (2014). Cell type-specific plasticity of striatal projection neurons in parkinsonism and L-DOPA-induced dyskinesia. Nat. Commun. 5, 5316. 10.1038/ncomms6316. [PubMed: 25360704]
72. D'Ascenzo M, Podda MV, Fellin T, Azzena GB, Haydon P, and Grassi C (2009). Activation of mGluR5 induces spike afterdepolarization and enhanced excitability in medium spiny neurons of the nucleus accumbens by modulating persistent Na+ currents. J. Physiol. 587, 3233–3250. 10.1113/jphysiol.2009.172593. [PubMed: 19433572]
73. Frick LR, Rapanelli M, Jindachomthong K, Grant P, Leckman JF, Swedo S, Williams K, and Pittenger C (2018). Differential binding of antibodies in PANDAS patients to cholinergic interneurons in the striatum. Brain Behav. Immun. 69, 304–311. 10.1016/j.bbi.2017.12.004. [PubMed: 29233751]
74. Xu J, Liu RJ, Fahey S, Frick L, Leckman J, Vaccarino F, Duman RS, Williams K, Swedo S, and Pittenger C (2021). Antibodies From Children With PANDAS Bind Specifically to Striatal Cholinergic Interneurons and Alter Their Activity. Am. J. Psychiatr. 178, 48–64. 10.1176/appi.ajp.2020.19070698. [PubMed: 32539528]
75. Abudukeyoumu N, Hernandez-Flores T, Garcia-Munoz M, and Arbuthnott GW (2019). Cholinergic modulation of striatal microcircuits. Eur. J. Neurosci. 49, 604–622. 10.1111/ejn.13949. [PubMed: 29797362]
76. Dautan D, Huerta-Ocampo I, Gut NK, Valencia M, Kondabolu K, Kim Y, Gerdjikov TV, and Mena-Segovia J (2020). Cholinergic midbrain afferents modulate striatal circuits and shape encoding of action strategies. Nat. Commun. 11, 1739. 10.1038/s41467-020-15514-3. [PubMed: 32269213]

77. Grybko MJ, Hahm ET, Perrine W, Parnes JA, Chick WS, Sharma G, Finger TE, and Vijayaraghavan S (2011). A transgenic mouse model reveals fast nicotinic transmission in hippocampal pyramidal neurons. Eur. J. Neurosci. 33, 1786–1798. 10.1111/j.1460-9568.2011.07671.x. [PubMed: 21501254]

78. Mei Y, Monteiro P, Zhou Y, Kim JA, Gao X, Fu Z, and Feng G (2016). Adult restoration of Shank3 expression rescues selective autistic-like phenotypes. Nature 530, 481–484. 10.1038/nature16971. [PubMed: 26886798]

79. Zhang Q, Gao X, Li C, Feliciano C, Wang D, Zhou D, Mei Y, Monteiro P, Anand M, Itohara S, et al. (2016). Impaired Dendritic Development and Memory in Sorbs2 Knock-Out Mice. J. Neurosci. 36, 2247–2260. 10.1523/jneurosci.2528-15.2016. [PubMed: 26888934]

80. Schneider CA, Rasband WS, and Eliceiri KW (2012). NIH Image to ImageJ: 25 years of image analysis. Nat. Methods 9, 671–675. 10.1038/nmeth.2089. [PubMed: 22930834]

81. Feng L, Zhao T, and Kim J (2015). neuTube 1.0: A New Design for Efficient Neuron Reconstruction Software Based on the SWC Format. eNeuro 2. 10.1523/eneuro.0049-14.2014.

Highlights

- SPNs in the dorsolateral striatum are hyperexcitable in *Sapap3*$^{-/-}$ mice
- Sapap3 deletion selectively elevates dendritic excitability in the direct pathway
- Evoked acetylcholine release in the dorsal striatum is elevated in *Sapap3*$^{-/-}$ mice
- Cholinergic signaling is differentially attenuated in both SPN populations

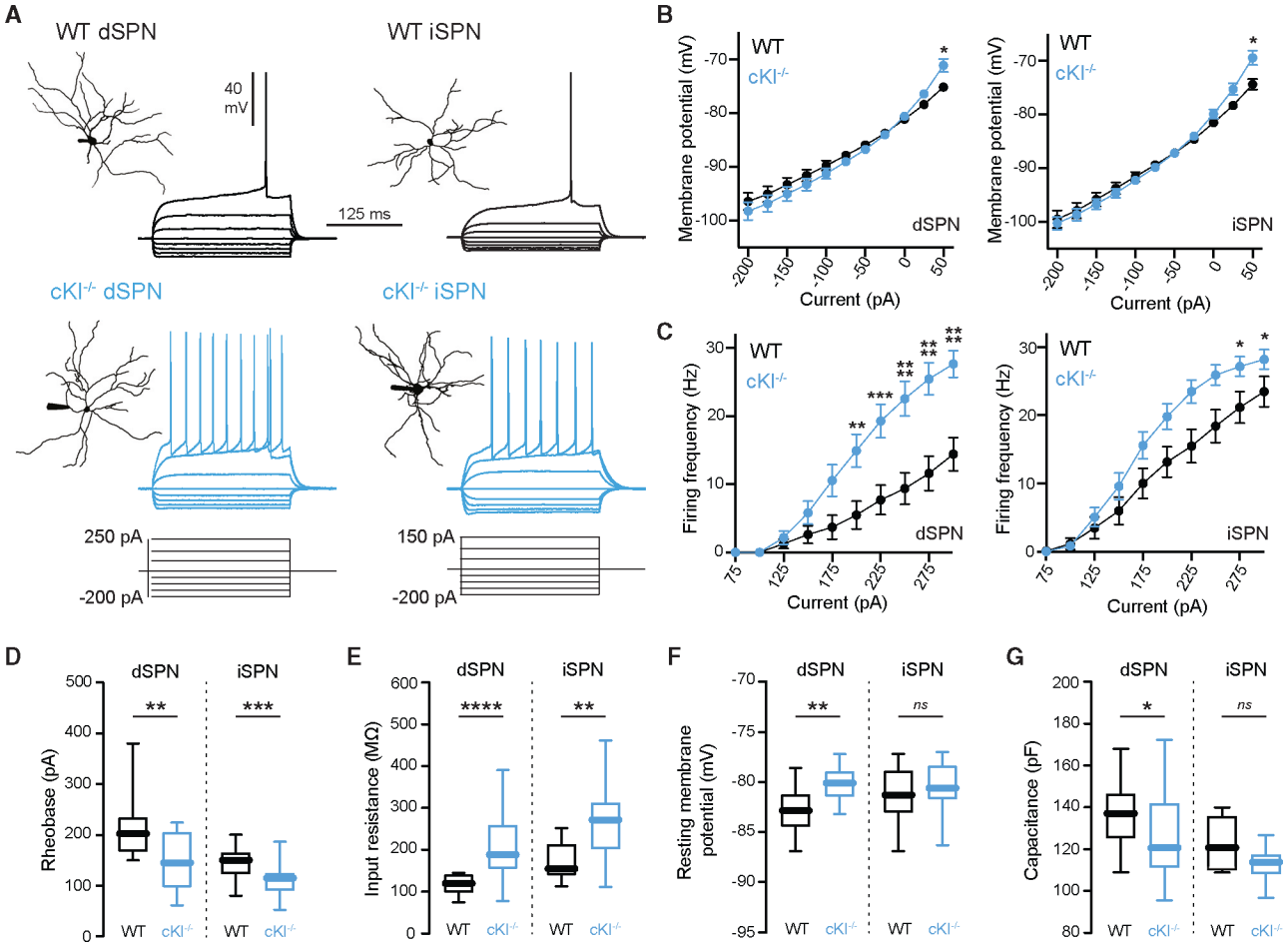

Figure 1. Increased somatic excitability of dSPNs and iSPNs in the dorsolateral striatum of SAPAP3 *cKI*$^{-/-}$ mice.

(A) Example anatomical reconstructions (left) and current-voltage (IV) traces (right) of WT (top; black) and *cKI*$^{-/-}$ (bottom; blue) dSPNs (left) and iSPNs (right).

(B) Quantification of steady-state voltage response to increasing subthreshold current injections in WT and *cKI*$^{-/-}$ dSPNs (left; WT n = 18, *cKI*$^{-/-}$ n = 16) and iSPNs (right; WT n = 15 cells, *cKI*$^{-/-}$ n = 19). *p < 0.05, two-way repeated measures ANOVA with Bonferroni's multiple comparisons test.

(C) Quantification of AP firing frequency in response to increasing current injections in WT and *cKI*$^{-/-}$ dSPNs (left; WT n = 19, *cKI*$^{-/-}$ n = 12) and iSPNs (right; WT n = 22 cells, *cKI*$^{-/-}$ n = 19). **p < 0.01, ***p < 0.001, and ****p < 0.0001, two-way repeated measures ANOVA with Bonferroni's multiple comparisons test.

(D) Boxplots showing rheobase currents in WT and *cKI*$^{-/-}$ SPNs. *dSPN*: WT n = 15 cells, *cKI*$^{-/-}$ n = 21; *iSPN*: WT n = 13, *cKI*$^{-/-}$ n = 24. **p < 0.01 and ***p < 0.001, Mann-Whitney.

(E) Boxplots showing input resistance in WT and *cKI*$^{-/-}$ SPNs. *dSPN*: WT n = 15 cells, *cKI*$^{-/-}$ n = 21; *iSPN*: WT n = 13, *cKI*$^{-/-}$ n = 21. **p < 0.01 and ****p < 0.0001, Mann-Whitney.

(F) Boxplots showing resting membrane potential in WT and *cKI*$^{-/-}$ SPNs. *dSPN*: WT n = 16 cells, *cKI*$^{-/-}$ n = 21; *iSPN*: WT n = 21, *cKI*$^{-/-}$ n = 27. **p < 0.01, ns, not significant, Mann-Whitney.

(G) Boxplots showing capacitance in WT and *cKI*$^{-/-}$ SPNs. *dSPN*: WT n = 15 cells, *cKI*$^{-/-}$ n = 20; *iSPN*: WT n = 9, *cKI*$^{-/-}$ n = 20. *p < 0.05, ns, not significant, Mann-Whitney.

All error bars are SEM. All boxplots are presented in Tukey style.

See also Figure S2.

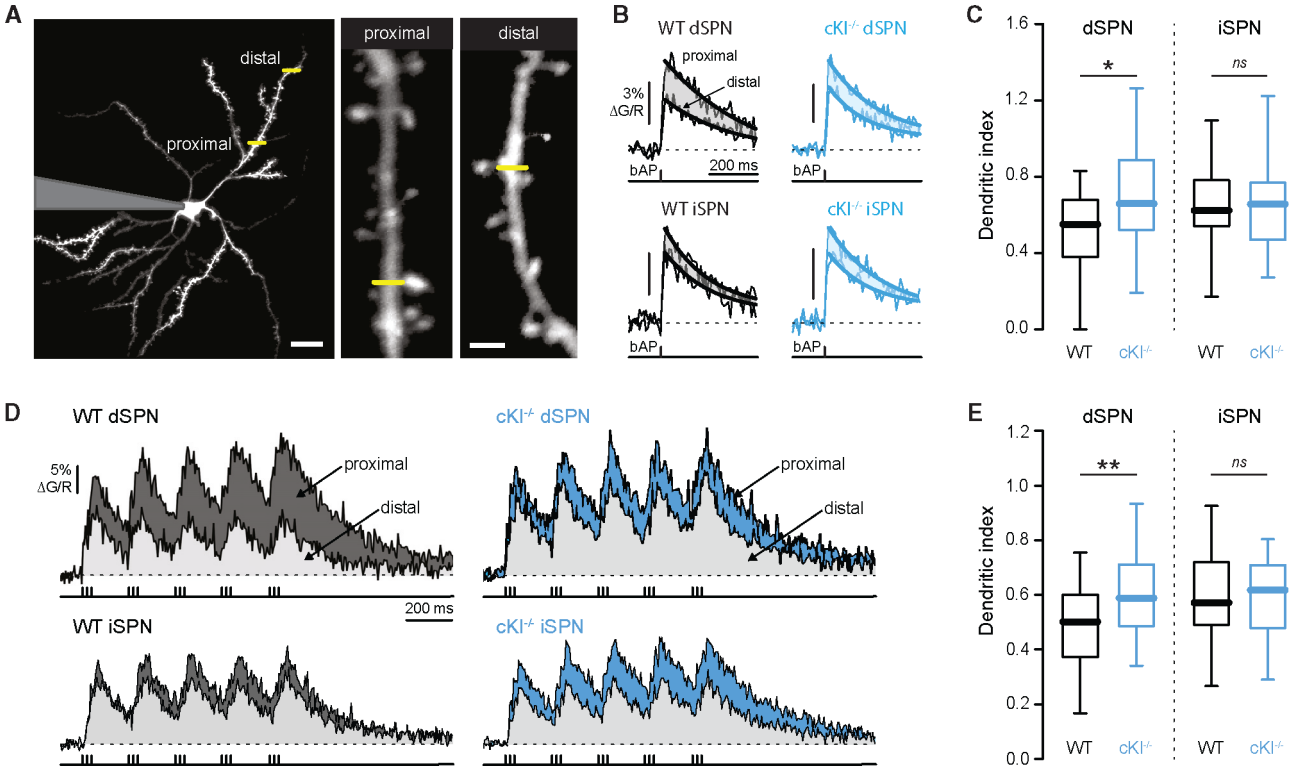

Figure 2. Dendritic excitability of dSPNs is increased in the dorsolateral striatum of SAPAP3 cKI$^{-/-}$ mice.

(A) 2-photon maximum intensity projection of a filled dSPN in a SAPAP3 *cKI*$^{-/-}$ × drd1-tdTomato mouse (scale bar: 20 μm); high-magnification images of proximal and distal dendrite line scan sites (yellow bars) are shown to the right (scale bar: 2 μm).

(B) Average proximal and distal dendritic Ca^{2+} transients with overlaid exponential fits (difference shaded) from WT (top; black) and *cKI*$^{-/-}$ (bottom; blue) dSPNs (left) and iSPNs (right) in response to single somatic bAPs (shown time-locked below traces).

(C) Boxplots of SPN dendritic indexes (ratio of distal:proximal bAP-evoked Ca^{2+} transients) in WT and SAPAP3 *cKI*$^{-/-}$ mice. *dSPN*: WT n = 31 dendrites, *cKI*$^{-/-}$ n = 31; *iSPN*: WT n = 30, *cKI*$^{-/-}$ n = 32. *p < 0.05, ns, not significant, Mann-Whitney.

(D) Average proximal and distal dendritic Ca^{2+} transients recorded from WT and SAPAP3 *cKI*$^{-/-}$ dSPNs and iSPNs in response to bursts of bAPs. Stimulus protocol eliciting bAPs shown time-locked below traces.

(E) Boxplots of SPN dendritic indexes in response to bursts of bAPs in WT and SAPAP3 *cKI*$^{-/-}$ dSPNs and iSPNs. *dSPN*: WT n = 34 dendrites, *cKI*$^{-/-}$ n = 42; *iSPN*: WT n = 29, *cKI*$^{-/-}$ n = 39. **p < 0.01, ns, not significant, Mann-Whitney.

All boxplots are presented in Tukey style.

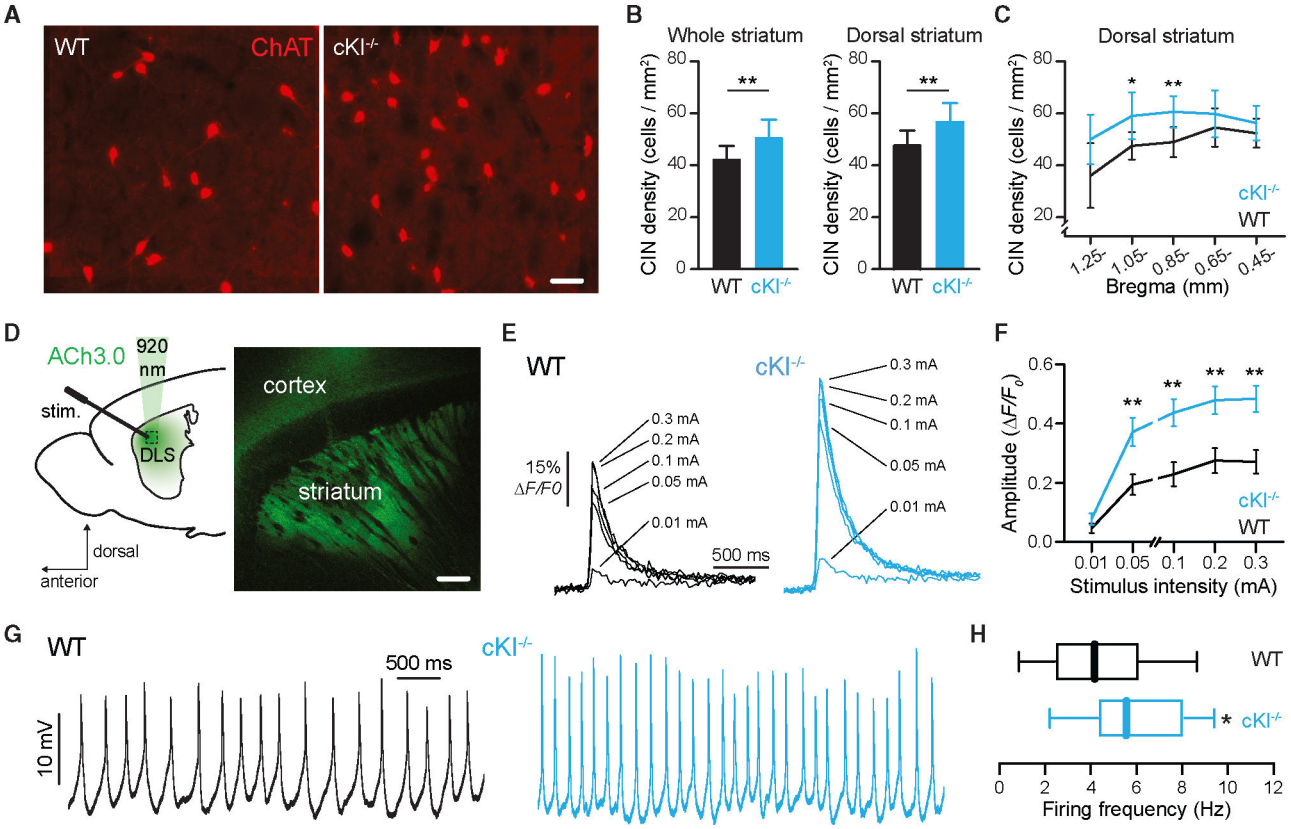

Figure 3. CIN density and evoked ACh release are increased in the dorsal striatum of SAPAP3 *cKI*$^{-/-}$ mice.

(A) Representative images showing choline acetyltransferase (ChAT) staining in the dorsolateral striatum of WT (left) and SAPAP3 *cKI*$^{-/-}$ (right) mice (scale bar: 50 μm).

(B) Bar graphs showing CIN soma densities in the entire striatum (left) and dorsal striatum (right) of WT (black; N = 10 mice) and SAPAP3 *cKI*$^{-/-}$ (blue; N = 11) mice. **p < 0.01, Mann-Whitney. Error bars are SEM.

(C) Line graphs showing CIN soma densities in the dorsal striatum of WT (black) and SAPAP3 *cKI*$^{-/-}$ (blue) mice binned rostro-caudally from bregma 1.25–0.25 mm. WT N = 10 mice, *cKI*$^{-/-}$ N = 11. *p < 0.05 and **p < 0.01, two-way repeated measures ANOVA with Bonferroni's multiple comparisons test.

(D) Schematic of experimental design used in (E) and (F) (scale bar: 100 μm).

(E) Average line scans measuring changes in ACh3.0 fluorescence in dorsal striatum neuropil of WT (black) and SAPAP3 *cKI*$^{-/-}$ (blue) mice in response to increasing electrical stimuli.

(F) Line graphs showing evoked ACh3.0 fluorescence amplitudes (calculated from exponential fits) at increasing stimulus intensities in WT (black) and SAPAP3 *cKI*$^{-/-}$ (blue) mice. WT n = 17 slices, *cKI*$^{-/-}$ n = 19. **p < 0.01, multiple Mann-Whitney tests.

(G) Representative cell-attached recordings of CIN pacemaking activity in the dorsal striatum of WT (black, left) and SAPAP3 *cKI*$^{-/-}$ (blue, right) mice.

(H) Boxplots of average ongoing CIN firing frequencies in the dorsal striatum of WT (black; n = 28 cells) and SAPAP3 *cKI*$^{-/-}$ (blue; n = 20) mice. *p < 0.05, Mann-Whitney.

All error bars are SEM. All boxplots are presented in Tukey style.

See also Figure S3.

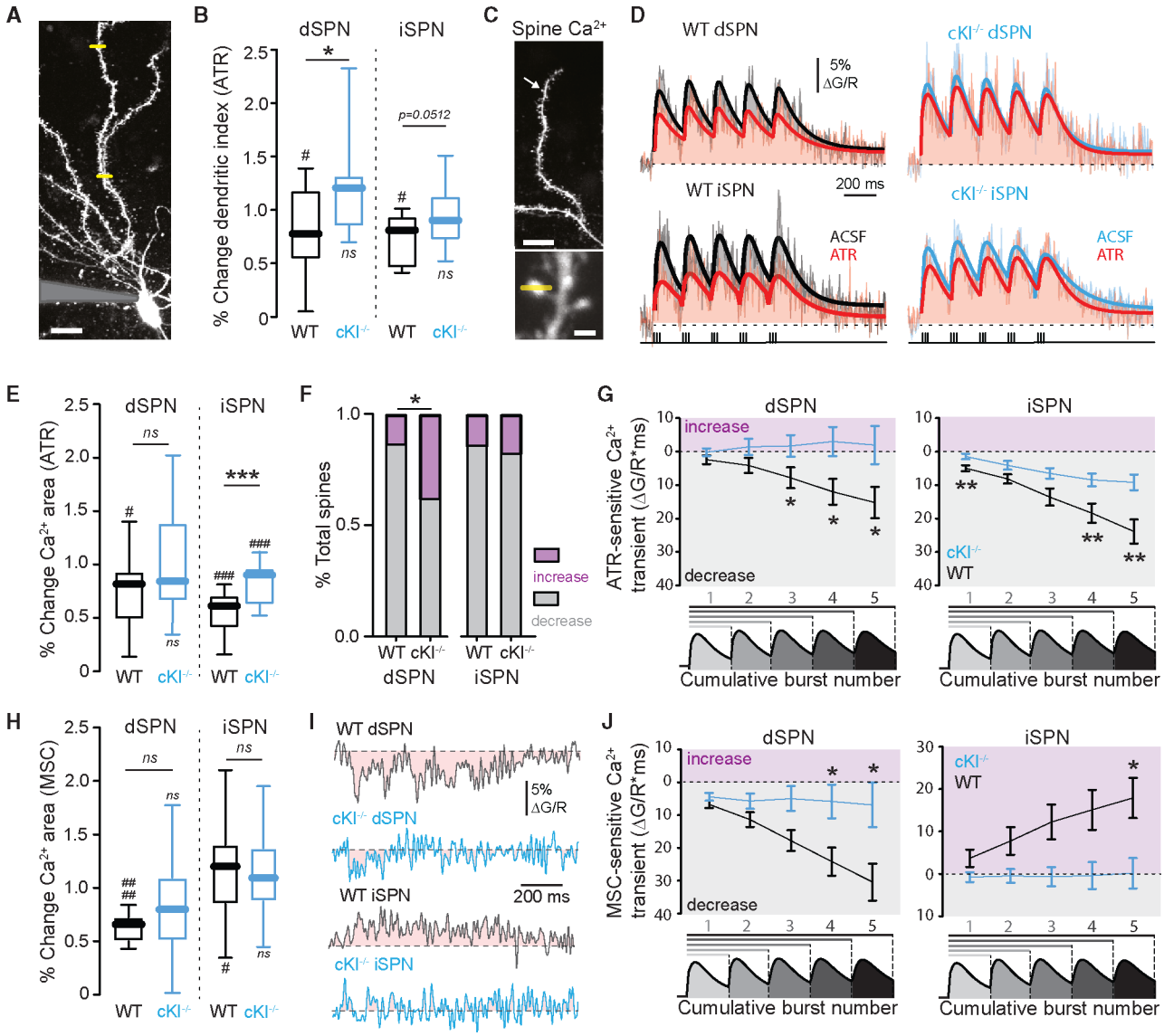

Figure 4. Muscarinic signaling is impaired in dSPNs and iSPNs of SAPAP3 *cKI*$^{-/-}$ mice.

(A) 2-photon maximum intensity projection of a filled dSPN (scale bar: 10 μm); sites of proximal and distal Ca^{2+} line scans are shown (yellow bars).

(B) Boxplots showing changes in SPN dendritic indexes (measured in response to bursts of bAPs) induced by atropine (10 μM) in WT and SAPAP3 *cKI*$^{-/-}$ mice. *dSPN*: WT n = 13 dendrites, *cKI*$^{-/-}$ n = 17; *iSPN*: WT n = 17, *cKI*$^{-/-}$ n = 13. A hash symbol (#) indicates a statistically significant difference between pre- and postatropine application; an asterisk (*) indicates a statistically significant difference between genotypes. #$p < 0.05$ and *$p < 0.05$, ns, not significant, Wilcoxon matched pairs.

(C) 2-photon maximum intensity projection of a filled dSPN dendrite (top; scale bar: 10μm). Arrow indicates location of high-magnification image (bottom; scale bar: 1 μm) of a distal dendritic spine and corresponding Ca^{2+} line scan (yellow bar).

(D) Average Ca^{2+} transients (evoked by bursts of bAPs) recorded from distal dendritic spines of WT and SAPAP3 *cKI*$^{-/-}$ dSPNs and iSPNs before (artificial cerebrospinal fluid [ACSF]) and after bath application of 10 μM atropine (ATR).

(E) Boxplots showing atropine-induced changes in Ca^{2+} transient areas (evoked by bursts of bAPs) in distal dendritic spines of WT and SAPAP3 *cKI*$^{-/-}$ dSPNs and iSPNs. *dSPN*: WT n = 18 spines, *cKI*$^{-/-}$ n = 15; *iSPN*: WT n = 14, *cKI*$^{-/-}$ n = 20. A hash symbol (#) indicates a statistically significant difference between pre- and postatropine application; an asterisk (*) indicates a statistically significant difference between genotypes. #$p < 0.05$, ###$p < 0.001$, and ***$p < 0.001$, ns, not significant, Wilcoxon matched pairs.

(F) Bar graphs showing fractions of total imaged spines whose bAP burst-evoked Ca^{2+} transients were increased (purple) or decreased (gray) by atropine. *dSPN*: WT n = 31, *cKI*$^{-/-}$ n = 24; *iSPN*: WT n = 22 spines, *cKI*$^{-/-}$ n = 35. *$p < 0.05$, Fisher's exact test.

(G) Line graphs showing the cumulative atropine-sensitive components of dendritic spine Ca^{2+} transients (post-minus preatropine traces) evoked by 5 successive bursts of bAPs. Integrated Ca^{2+} transients were divided into segments corresponding to each of the 5 successive bursts (diagrammatically shown in register below). The y axis is reported as absolute values of positive areas (indicating a net atropine-induced decrease; gray) and negative areas (indicating a net atropine-induced increase; purple). *dSPN*: WT n = 18 spines, *cKI*$^{-/-}$ n = 15; *iSPN*: WT n = 14, *cKI*$^{-/-}$ n = 20. *$p < 0.05$, **$p < 0.01$, Mann-Whitney.

(H) Boxplots showing muscarine-induced changes in Ca^{2+} areas (evoked by bursts of bAPs) in distal dendritic spines of WT and SAPAP3 *cKI*$^{-/-}$ dSPNs and iSPNs. A hash symbol (#) indicates a statistically significant difference between pre- and postmuscarine application. dSPN: WT n = 21 spines, *cKI*$^{-/-}$ n = 20; *iSPN*: WT n = 21, *cKI*$^{-/-}$ n = 21. #$p < 0.05$ and ####$p < 0.0001$, ns, not significant, Wilcoxon matched pairs.

(I) Averaged muscarinic components (post-minus premuscarine traces) of Ca^{2+} transients evoked by bAP bursting. Areas shaded to zero (red).

(J) Line graphs showing the cumulative muscarine-sensitive components of dendritic spine Ca^{2+} transients (post-minus premuscarine traces) evoked by 5 successive bursts of bAPs. Integrated Ca^{2+} transients were divided into segments corresponding to each of the 5 successive bursts (diagrammatically shown in register below). The y axis is reported as absolute values of positive areas (indicating a net muscarine-induced decrease; gray) and negative areas (indicating a net muscarine-induced increase; purple). *dSPN*: WT n = 21 spines, *cKI*$^{-/-}$ n = 19; *iSPN*: WT n = 17, *cKI*$^{-/-}$ n = 25. *$p < 0.05$, Mann-Whitney.

All error bars are SEM. All boxplots are presented in Tukey style.

See also Figure S4.

KEY RESOURCES TABLE

REAGENT or RESOURCE	SOURCE	IDENTIFIER
Antibodies		
Goat anti-ChAT	EMD Millipore	ab144P; RRID: AB_2079751
Donkey anti-goat Alexa Fluor™ 594	Abcam	ab1501132; RRID: AB_2810222
Rabbit anti-μ-opioid receptor	Abcam	ab10275; RRID: AB_2156356
Donkey anti-rabbit 488	Invitrogen	A-21206; RRID: AB_2535792
Rabbit anti-SAPAP3	G. Feng	https://doi.org/10.1002/cne.20060
Mouse anti-β-actin	Sigma	A5441; RRID: AB_476744
Bacterial and virus strains		
AAV5-hSyn-ACh3.0(ACh4.3)	WZ Biosciences	https://www.wzbio.com/aavGrab.php?pid=4&id=4&cid=90&page=11
Chemicals, peptides, and recombinant proteins		
Alexa Fluor™ 568 Hydrazide	Invitrogen	https://www.thermofisher.com/order/catalog/product/A10437
Atropine sulfate	Sigma-Aldrich	CAS# 5908–99-6
Fluo-4 pentapotassium salt	Invitrogen	https://www.thermofisher.com/order/catalog/product/F14200?SID=srch-srp-F14200
Mecamylamine hydrochloride	Sigma-Aldrich, TOCRIS	CAS# 826–39-1
Muscarine chloride	Sigma-Aldrich	CAS# 2303–35-7
Muscarine iodide	TOCRIS	CAS# 24570–49-8
Scopolamine hydrobromide	TOCRIS	CAS# 114–49-8
Isoflurane	Covetrus	CAS# 26675–46-7
Meloxicam	Covetrus	CAS# 71125–38-7
Experimental models: Organisms/strains		
Mouse: B6.Cg-Tg(Drd1a-tdTomato)6Calak/J	Jackson Laboratories	RRID: IMSR_JAX:016204
Mouse: B6; Tg(Drd2-eGFP) S118Gsat/Mmnc	GENSAT	RRID: MMRRC_000230-UNC
Mouse: Tg(Chat-tau/EGFP)#Svj	(Grybko et al.)[77]	MGI: 5605267
Mouse: C57BL/6J	Jackson Laboratories	RRID: IMSR_JAX:000664
Mouse: B6.Cg-Tg(ACTFLPe)9205Dym/J	Jackson Laboratories	RRID: IMSR_JAX:005703
Mouse: B6 SAPAP3 cKI$^{-/-}$	G. Feng and Q. Zhang	N/A
Software and algorithms		
Adobe Illustrator	Adobe	RRID: SCR_010279 https://www.adobe.com/products/illustrator.html
EthoVision XT	Noldus Information Technology	RRID: SCR_000441 https://www.noldus.com/ethovision-xt
GraphPad Prism v10	GraphPad Software	RRID: SCR_002798 https://www.graphpad.com/how-to-buy/
Igor Pro	WaveMetrics, Inc.	RRID: SCR_000325 https://www.wavemetrics.com/products/igorpro
ImageJ	(Schneider et al.)[80]	RRID: SCR_003070https://fiji.sc

REAGENT or RESOURCE	SOURCE	IDENTIFIER
MATLAB R2023b	MathWorks	RRID: SCR_001622 https://www.mathworks.com/products/matlab.html?s_tid=hp_products_matlab
Mini Analysis	Synaptosoft	RRID: SCR_002184
neuTube	(Feng et al.)[81]	https://neutracing.com
Prairie View v5.4	Bruker Nano, Inc.	RRID: SCR_017142
Angle Two™	Leica Biosystems	https://www.leicabiosystems.com/sites/default/files/media_product-download/2021-02/Leica_Angle_Two_User_Manual.pdf
Other		
VT1000 S vibrating blade microtome	Leica Biosystems	RRID: SCR_016495
MultiClamp 700B microelectrode amplifier	Molecular Devices, LLC	RRID: SCR_018455
Concentric bipolar electrode	FHC	https://www.fh-co.com/product/concentric-bipolar/
ISO-Flex stimulus isolator	Microprobes for Life Sciences	RRID: SCR_018945
Bruker Ultima laser scanning microscope	Bruker Nano, Inc.	RRID: SCR_019800
VS.120-S6-W virtual slide microscope	EVIDENT/Olympus	RRID: SCR_018411
Angle Two™ stereotaxic instrument	Leica Biosystems	https://www.leicabiosystems.com/us/research/neuroscience/angle-two-small-animal-stereotaxic-instrument/
Quintessential stereotaxic injector (QSI™)	Stoelting Co.	https://stoeltingco.com/Neuroscience/Stoelting-Quintessential-Stereotaxic-Injector-QSItm~9751?navigate_from_document = 1022&navigated_from_object = 3840
Artificial tears lubricant ophthalmic ointment	Covetrus	NDC: 11695–6832-1
Fluoromount-G	SouthernBiotech	RRID: SCR_015961